

A Robust and Reliable Climbing Robot for Steel Structure Inspection

Anh Q. Pham, Cadence Motley, Son T. Nguyen, Hung M. La, *IEEE Senior Member*

Abstract—This paper presents a new, robust and reliable robot capable of carrying heavy equipment loads without sacrificing mobility that can improve the safety and detail of steel inspections in difficult access areas. In addition, the robot functions with an embedded NORTEC 600, eddy current sensor, and a GoPro camera that allows it to conduct nondestructive evaluation and collect high-resolution imagery data of steel structures. The data is processed into a heatmap for quick and easy interpretation by the user. In order to verify the robot's designed capabilities, a set of mechanical analyses were performed to quantify the designed robot's limits and failure mechanics. The application of our robot would increase the safety of an inspector by reducing the frequency they would need to hang underneath a bridge or travel along a narrow section. Demonstration of the robot deployments can be seen in this link: <https://youtu.be/8d78d7CWXYk>

I. INTRODUCTION

In total, there are 175,825 bridges in the United States that have main spans primarily made of steel [1]. Of these bridges, just over 50% of them were made 50 or more years ago. Many of the country's steel bridges have also become functionally obsolete as the design standards behind the civil engineering of bridges have risen, and time has passed [2]. The 2017 infrastructure report card created by the American Society of Civil Engineers states that "9.1% of the nation's bridges were structurally deficient in 2016" [3]. As time continues to pass, the situation is bound to intensify so long as significant action is not taken to renew the aging infrastructure. While the nation fails to address the core issue, work can be done to improve the efficiency of what is being done, inspections, and repairs. The current practice of steel bridge inspection is mainly performed manually by well-trained bridge engineers. This process is time-consuming, not efficient, and often dangerous for the inspectors since they have to climb high structures (e.g., Fig. 1).

The state and capabilities of bridge inspection robots are rapidly developing as showcased by [5]–[19]. Recent progress in the field of steel bridge inspection includes the

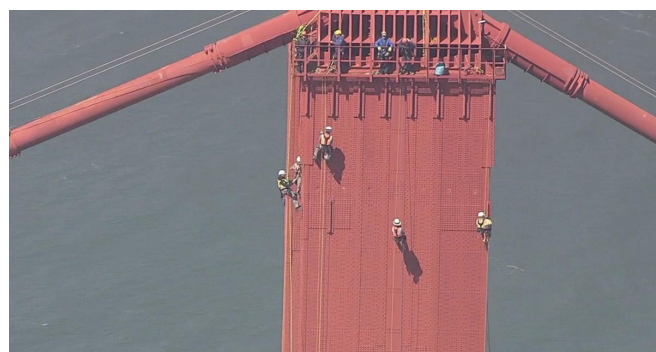


Fig. 1: Manual inspection of the Golden Gate Bridge in San Francisco on May 3, 2018. Source: CBSNews [4].

creation of MINOAS [17] in 2012, CROC [12] in 2015, BIREM [16] in 2017, multiple different types of steel climbing robots from the Advanced Robotics and Automation (ARA) lab recently [20]–[30]. Each of these robots takes its own unique approach toward conducting and gathering useful information for steel bridge inspection.

MINOAS, is a marine inspection robotic assistant created to traverse the underside of boats with steel hulls [17]. The robot makes use of two large wheels with magnets at the extremities and a third wheel, which is used to stabilize the design when on steel surfaces. The robot is designed to provide detailed imagery and measure the thickness of the steel at particular locations. However, it seems quite clear based on demonstrations that the robot is at risk of falling if it gathers too much momentum when moving downward, and it is also clear that the robot cannot carry much more of an equipment load than it was designed to carry.

BIREM is a robot designed by the Department of Mechanical and Physical Engineering at Osaka City University in Japan. This robot was created to be quite small at a size of $245\text{mm} \times 80\text{mm} \times 133\text{mm}$ and was designed to be able to navigate between the bolt spacing that is standard in Japan's bridges [16]. At its current progress, this robot only collects visual data of the steel surfaces that it traverses. Since BIREM was designed to travel between nuts, this robot is most effective when passing or inspecting splices on steel bridges. Due to its size, though, this robot cannot be outfitted with additional inspection equipment since it would not fit, and its adhesion strength is not strong enough to support a significant amount of increased mass.

Back in 2015-2017, the University of Technology Sydney created a groundbreaking robot meant to function on and inspect steel bridges [12], [31]–[33]. CROC was designed to traverse steel structures similar to how an inchworm would.

This work was funded by Vingroup Joint Stock Company and supported by Vingroup Innovation Foundation (VINIF) under project code VINIF.2020.NCUD.DA094, the U.S. National Science Foundation (NSF) under grants NSF-CAREER: 1846513 and NSF-PFI-TT: 1919127, and the U.S. Department of Transportation, Office of the Assistant Secretary for Research and Technology (USDOT/OST-R) under Grant No. 69A3551747126 through INSPIRE University Transportation Center. The views, opinions, findings and conclusions reflected in this publication are solely those of the authors and do not represent the official policy or position of the VINIF, the NSF, and the USDOT/OST-R.

Anh Pham is with the AIR-VIET Corporation, Vietnam. Cadence Motley, Son Nguyen and Hung La are with the Advanced Robotics and Automation (ARA) Lab, Department of Computer Science and Engineering, University of Nevada, Reno, NV 89557, USA. Corresponding author: Hung La, email: hla@unr.edu.

The design has two large foot pads with neodymium magnets on them. This robot collects image data of the bridge, is capable of traversing tight spaces, and also creates a 3D map of the structure that it has passed through. The most significant limitation of this robot is that it can not travel very quickly and is tethered to a power source. This could quickly become an issue in cases where the robot travels around a corner or needs to go further out than the tether would permit.

While each of these robots makes their vital contributions to a robotic inspection of steel, none of the robots created so far have been able to carry heavy equipment loads and maintain their ability to traverse around steel members quickly. Most current works are only capable of gathering superficial data like imagery. However, our robot can utilize the embedded equipment to gather fatigue cracking data in steel, is not tethered, can carry large loads, is still mobile, and gathers visual data with high-resolution cameras.

In this paper, we present a new, robust and reliable robot, which:

- is mobile and carries large loads,
- has an embedded Nortec 600 eddy current sensor,
- gathers visual, eddy current and IMU/encoder data,
- generates heatmaps with collected data.

In addition to the practical contribution of this robot to the bridge inspection, a scientific contribution lies in a detailed analysis of the mechanics of the robot, which was performed to discern its mechanical limits and worst-case scenario failure mechanics. Both turn-over and sliding friction analyses are carefully investigated to ensure the robot works well in various steel structure environments. Moreover, a new contact stress analysis was performed on our robot's contact points to analyze better the failure conditions of the neodymium ring magnet wheels. This two-part analysis in static and dynamic conditions informed us about the forces acting on the robot's wheels and the failure conditions that could damage them.

II. OVERALL DESIGN

To start, we identified a few design parameters to help us design the capabilities of the proposed robot. These parameters were to create a robot, which was sturdy and straightforward to use, could function autonomously, could be outfitted with additional equipment, and was mobile.

Overall, the ARA robot in Fig. 2 consists of an aluminum frame and a scanning frame made of hardened steel rods. The frame (see Fig. 3) has a belt system on it used to maneuver an eddy current probe around a scanning area. There are four large ring magnets, which make up the inside of the robot's wheels. Each magnet generates an attractive force of 1126.7 N. On top of the frame above the wheels lies the computer, which controls the wheels, camera, and stepper motors. On the very top is where the NORTEC 600 rests securely, it is a device for eddy current flaw detection. When scanning, the eddy current probe is moved in a line-by-line pattern throughout the scanning area. The robot is powered with LiPo batteries and has a run time of 60 minutes before

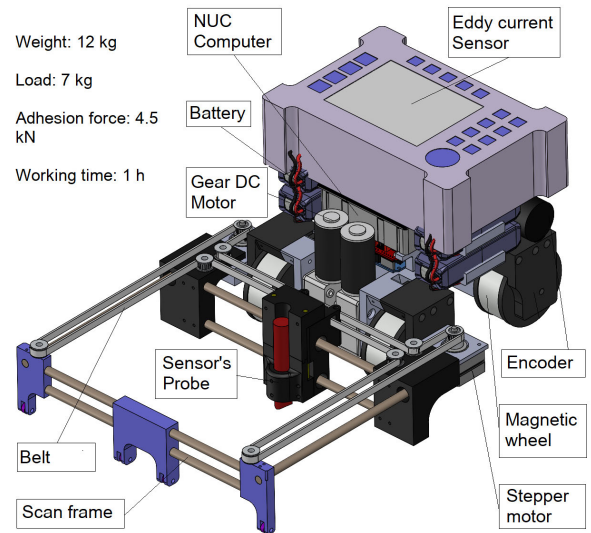


Fig. 2: CAD model and specifications of the proposed ARA robot.

needing to recharge. The robot is attached to a work surface by carefully placing it onto the steel until the magnets pull the robot in or through the use of a ramp to allow the robot to roll down and onto the steel. The robot is removed from its work surface by making use of this ramp as well.

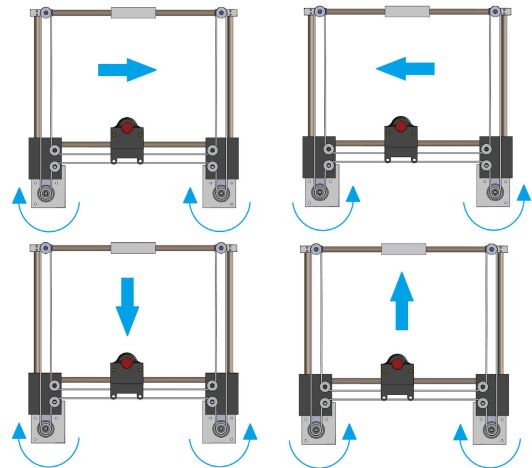


Fig. 3: H-belt drive is applied for scan mechanism. The moving of probe is combined between two stepper motors. The mechanism is light and simple, which help reduce robot's weight.

The manufactured robot has an aluminum frame consisting of an area of $20.5\text{cm} \times 18.7\text{cm}$ with a thickness of 1.2cm or greater. The scanning area is $17.6\text{cm} \times 16.76\text{cm}$ and overall, the robot takes up a space of $45.65\text{cm} \times 31.2\text{cm} \times 21.73\text{cm}$. Two limit switches were created by adding two aluminum strips to complete a circuit when the robot's eddy current probe is at the home position for each dimension of travel in the x and y .

Figure 4 shows the electrical structure and connectivity of the proposed robot, which is equipped with four servos, two encoders, an IMU, a camera, a NUC computer running ROS, and a NORTEC 600. There are two boards, the main, which controls the wheels of the robot and receives the encoder and

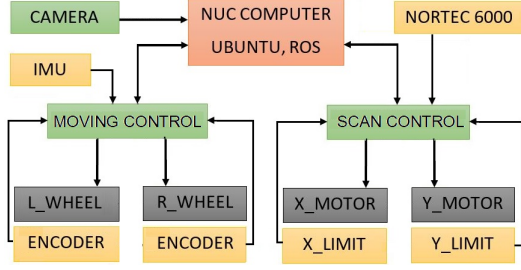


Fig. 4: ROS program on NUC computer works as high-level control. It reads remote control signal (in tele-operation mode), sends the command to moving and scan nodes (low level control), captures live camera then sends to ground station, calculates path planning algorithm [26] based on odometry feedback node (in auto navigation mode), and saves collected data. Moving control node (Arduino Mega) receives a command from computer to control speed motors, besides reading encoders and IMU feedback then sends back to Odom node. Scan node (Arduino Uno) receives the command start, calculates the scanning path, exports signal to control stepper motors, and reads data from Nortec 600, then sends back to data saving mode.

IMU data, and the sensor board controls the motors, which allow the robot to scan with the eddy current sensor from the NORTEC 600. 11.1 V lithium polymer batteries power the electrical components.

III. ANALYSIS OF ROBOT DESIGN

A set of analyses was done to assess the durability of the created robot. From the assessments, it has been found that the proposed robot is substantially over-fitted with a bulky frame and magnets, which border overkill. However, this redundancy was intentional to create a robot, which would be operable by a much larger demographic than just trained and certified inspectors. With this in mind, extra redundancy is in order to ensure that the expensive equipment housed on the proposed robot is never damaged, lost or destroyed while still being capable of obtaining a collection of useful data (fatigue cracking, imagery, location) on the steel that the robot is inspecting.

A. Turn Over Analysis

The purpose of a turn-over analysis is to analyze how well an inspection robot will be able to adhere to a surface. The parameters (see Fig. 5), which have an especially large role in this analysis are contact points (A, B) spacing d_2 [x,y] (where the wheels touch the steel relative to each other), distance of the center of gravity (COG) in the direction d_3 [z] that is going out of the contact plane [x,y], and the force output of each magnet into the contact plane $F_{A\text{mag}}$ and $F_{B\text{mag}}$ [-z].

To optimize, a designer should minimize the COG's distance from the contact plane d_3 and maximize the spacing between contact points (d_2) and the forces of each magnet set $F_{A\text{mag}}$ and $F_{B\text{mag}}$. Practically speaking, this can only be done to a certain extent before the robot's functionality is compromised. This is where the need for design and analysis comes into play. A robot with an extensive breakdown of how it will interact with its environment is essential for creating a robot that will function as intended consistently. d_1 is half of the thickness of the lowest wheel. The two d_2 values were

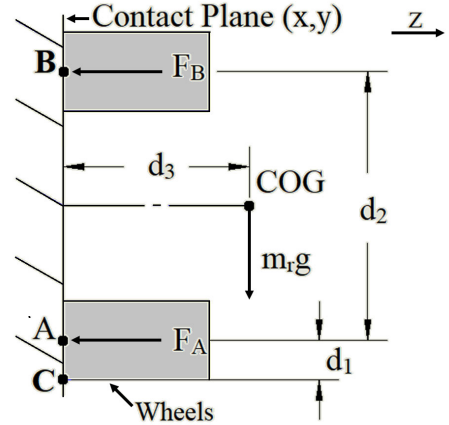


Fig. 5: Generic Robot on Wall Diagram. The left-most line represents a fixed surface (plane) to which the robot is adhered to. A rotation about the z-axis of 90 degrees will shift the robot's axis, supporting the weight and changing some of the distances at play in the equations. (Creating two d_2 s for instance.)

picked to ensure that our robot could fit inside the channel of I beams and ensure that our robot could accommodate all of the embedded equipment inside it.

In order to discern the threshold of the capabilities for the proposed robot, a turn over analysis was performed through an application of statics [$\sum_{i=1}^n F_i = 0$, $\sum_{i=1}^n M_i = 0$]. By calculating the summation of moments acting on the robot at point C, we can derive the following equations for two instances of positioning of the robot. The first (1) when the robot is traveling horizontally (in and out of the paper/diagram) and the second (2) when the robot is traveling vertically ($d_2 = 14.706\text{cm}$) and is parallel ($d_2 = 7.188\text{cm}$) to the field of gravity acting on it (up and down the paper/diagram).

$$0 = d_1(2F_{A\text{mag}}) + (d_1 + d_2)(2F_{B\text{mag}}) - d_3m_r g - M_C. \quad (1)$$

By solving for M_C from Equ. 1, we can calculate the maximum external moment that can be applied to the robot before it will turn over, off of the surface it is adhered to. Anything under this threshold will not cause the robot to fall. This value M_C is effectively the surplus moment that the robot is not utilizing. In further equations M_{sur} will be used in place of M_C . A maximum equipment load can be determined, assuming the COG does not change as a result of the added mass. The resulting equation to solve for this is as follows:

$$m_e = \frac{M_{\text{sur}}}{d_3 g}, \quad (2)$$

where m_e is the maximum equipment load the constructed robot is capable of carrying, assuming that the COM does not change, and M_{sur} is the smallest surplus of moment determined from the vertical and horizontal analyses. Using Equ. 1 we were able to discern that the robot is capable of carrying an additional maximum mass of 93.8 kg, assuming static conditions regarding the robot's ability to resist turning over. Please note that surplus variables (M_{sur} , $F_{A\text{sur}}$, $F_{B\text{sur}}$) are worst-case scenarios under the assumption that the robot

is loaded with the maximum functioning equipment load under the above assumptions.

B. Contact Stress Analysis

To ensure that the wheels of the proposed robot would not break or shatter from the wear and tear of use and work accidents, an analysis has been done to assess the durability and strength of the robot's wheels. Two major assessments were done, the first under static conditions and the second under dynamic conditions, as presented below.

1) *Static Contact Stress Analysis:* This static analysis builds on the equations derived from the Turn Over Analysis and the same set of diagrams. A summation of forces is done for each case, 1 (vertical) and 2 (horizontal). This yields the following equation:

$$0 = 2F_{Amag} + 2F_{Bmag} - F_{Asur} - F_{Bsur}. \quad (3)$$

By solving this equation for F_{Asur} and plugging it into the Moment Equ. 1 where F_{Amag} , F_{Bmag} and M_C are replaced with F_{Asur} , F_{Bsur} and M_{sur} in Equ. 1. The reactionary forces F_{Asur} and F_{Bsur} acting at points A and B in the opposite direction of F_{Amag} and F_{Bmag} can be solved for and calculated. The equation to determine F_{Bsur} is as follows. The highest reactionary value calculated was F_{Asur} in Case 2 (Horizontal) at 3.78 kN.

$$F_{Bsur} = \frac{M_{sur} - 4d_1(F_{Amag} + F_{Bmag}) + d_3m_r g}{2d_2}. \quad (4)$$

Next, the half-width of the contact area must be calculated where b is the half-width of the deformation, which occurs between the wheels and the steel plate due to force F .

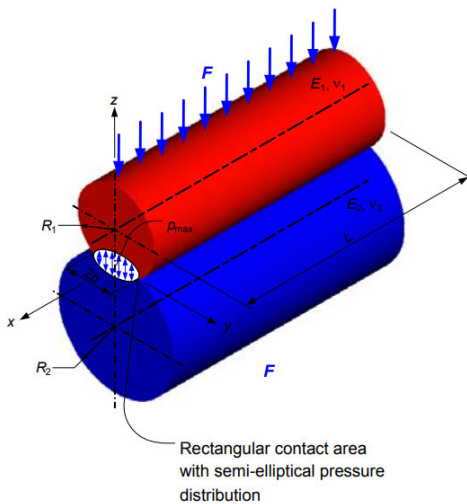


Fig. 6: Generic contact stress diagram [34].

In Fig. 6, L is the width of the wheel, v is Poisson's ratio of the material, E is the modulus of elasticity of the material, and F is F_{Asur} , which is the highest reactionary force acting on any of the wheels for all cases. To create the scenario of a plate (steel surface (subscript $[_2]$)) in contact with a cylinder

(wheel (subscript $[_1]$)), R_2 is set to be infinity, to create the scenario of a cylinder in contact with a flat surface.

$$b = \sqrt{\frac{4F(\frac{1-v_1^2}{E_1} + \frac{1-v_2^2}{E_2})}{\pi L(\frac{1}{R_1} + \frac{1}{R_2})}}. \quad (5)$$

Once the half width has been calculated with Equ. 5, we can then calculate how much stress the wheels are under. This can be done with the following contact stress equation:

$$p_{max} = \frac{2F}{\pi Lb}. \quad (6)$$

The calculated p_{max} value from Equ. 6 is then compared with the compression strength of the material of the wheels. We are using neodymium magnets of grade N-42, with a corresponding compression strength of 950 MPa. The maximum value calculated for p_{max} under static conditions is 59.75 MPa, which is significantly smaller than the neodymium magnets compression strength. This means that the wheels will not break from the stresses during normal use in static conditions.

2) *Dynamic Contact Stress Analysis:* This analysis was done to better understand how durable the robot's neodymium magnet wheels would be when it is being put down or dropped on a steel surface. This analysis is particularly important for these wheels since neodymium magnets are quite brittle. As a result, any failure would more than likely decommission the robot until it can be repaired with a new wheel. Assuming that all of the assumptions made during this calculation do not neglect a major factor of this analysis, we were able to determine that the robot's maximum drop height that would not result in breakage of the wheels is at approximately 0.1868 meters.

To perform this analysis, we would need to calculate how quickly the robot would be moving until it impacted the steel. The two major contributing elements to the velocity of the robot at the time of impact are the height at which the robot is dropped and the relative pull strength of the neodymium magnet at some distance h at time t . Assuming that the robot starts with no initial velocity and at a distance that is further than the magnets pull range ($F_{mag} = 0$ at $t = 0$). The velocity at $h = 0$ can be calculated by summing the velocity added by force generated from the magnetic fields V_{mag} , at time t and distance h and the velocity added through the force of gravity V_{height} , over the whole drop distance. These equations are as follows:

$$V_{height} = -\sqrt{2gh}, \quad (7)$$

$$V_{mag} = \frac{1}{m_r} \int_0^t F_{mag}, \quad (8)$$

where $F_{mag} = f(h)$. To simplify Equ. 8, we made two assumptions, that the force of the magnetic field was a

constant equal to $\frac{3}{4}F_{mag}$ and that the duration of time F_{mag} acts is 0.1s. This allowed us to simplify the V_{mag} equation and calculate the robots initial velocity, V_i going into the impact.

$$V_{mag} = \frac{3F_{mag}t}{4m_r}. \quad (9)$$

$$V_i = V_{height} + V_{mag}. \quad (10)$$

After determining the initial velocity of the robot going into an impact with a steel plate, we had to calculate the average force that would act on the robot due to the collision. The generic equation for impulse momentum is as follows:

$$\int_0^t F dt = m_r V_f - m_r V_i. \quad (11)$$

Since the magnet is strongly attracted to the steel surface, and the steel plate is not going to move, we can assume that the impact occurs over a very small amount of time like 0.0001s, and that the final velocity of the robot V_f will be 0. This equation then simplifies down to:

$$F_{avg} \Delta t = -m_r V_i. \quad (12)$$

Armed with the average force, which acts on the wheels during the course of the robots impact with the steel plate, we can now substitute F with F_{avg} in Eqs. 5 and 6 to calculate the stress, which acts on the wheels from height h . When solving for h_{max} the following equation is obtained by utilizing Eqs. 5, 6, 7, 9 and 12:

$$h_{max} = \frac{\left(\frac{\pi \sigma_c b L \Delta t}{m_r} - V_{mag}\right)^2}{2g}. \quad (13)$$

Unfortunately, Equ. 13 for h_{max} cannot be used since b is dependent on F_{avg} , which is dependent on h_{max} . From here, we concluded that they would need to iteratively solve for h_{max} if they wanted to obtain an answer. We created a MATLAB code, which utilized these equations and iteratively changed h in order to make p_{max} from Equ. 6 equal to the compression strength of the neodymium magnets, 950 MPa. Once the resulting p_{max} value determined from h had converged to σ_c , the team was able to effectively determine h_{max} for which the robot could be dropped from without suffering any breakage in the neodymium wheels of the created robot. The resulting h_{max} value the robot could be dropped from is 0.1868m.

C. Sliding Friction Analysis

After determining the durability of the proposed robot's wheels, another statics analysis was done to quantify the robot's ability to stay in place when resisting gravity on a steel beam. The equation for the force of friction of the robot is determined.

$$F_F = N\mu - (m_r + m_e)g|\sin(\theta)|. \quad (14)$$

Where N is the normal force acting on the wheels, μ is the friction coefficient between the wheels and the steel surface, and θ is the angle of orientation the robot is in. The net normal force acting on the robot can be written as the sum of the attractive forces from the neodymium magnets plus or minus the force of gravity acting on the robot with the maximum equipment load calculated from Equ. 2 ($m_e = 93.8kg$).

$$N = 2F_{A_{mag}} + 2F_{B_{mag}} + (m_r + m_e)g\cos(\theta). \quad (15)$$

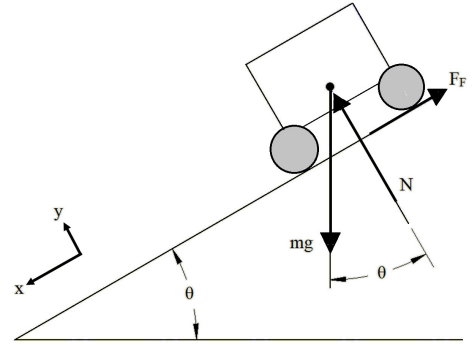


Fig. 7: Determination of friction coefficient diagram.

To design the robot in a robust manner, both worst case scenarios ($\theta = 90^\circ$ & 180°) are considered in order to discern the limits of the robot. This when the robot is oriented parallel to gravity ($\theta = 90^\circ$) and completely upside down ($\theta = 180^\circ$).

From here, we needed to perform an experiment shown in Fig. 7 to figure out what the friction coefficient is between the two surfaces. This can be done by getting a steel beam, a piece of mass with the sandpaper on one side, and an angle measurement device. The friction factor can be determined by placing the mass on the steel beam, sandpaper side down, and raising one side of the beam until the mass moves. The tangent of this angle is the friction factor of the two materials when in contact. This experiment yielded a friction coefficient of 0.44084 between the steel and the sandpaper. Using the coefficient of friction and net normal force values in Equ. 14 yield results for the force of friction ($\theta = 90^\circ$, $F_F = 880.27N$ and $\theta = 180^\circ$, $F_F = 1529.3N$).

Since none of the results obtained for the force of friction are negative, we can conclude that the limiting factor of the design of our robot is from the Turn Over Analysis scenario, Equ. 2. This offers invaluable insight into the primary failure condition of our robot and information about the forces required to move the robot manually when it is on a surface.

When experimenting to determine the coefficient of friction between the steel and sandpaper, the data set retrieved had a variation of ± 0.0107 . A simple average of the data set from a total of 12 experiments was taken as the value for the coefficient of friction ($\mu = .44084$).

IV. FIELD DEPLOYMENT AND VERIFICATION

Once the robot had successfully been designed, manufactured, built, and programmed, we decided to run field



Fig. 8: Adhesion test: a woman (weight of 64kg) hanging from robot adhered to steel I beam. The robot's adhesion force is significantly stronger than the force that multiple people can exert combined is.



Fig. 9: Robot testing on a curved steel surface.



Fig. 10: Robot testing on perforated surface.

tests on the created robot. Since the robot's adhesion force is significantly stronger than the force that multiple people can exert combined is, we decided that simple proofs of concept of the robot functioning on various steel surfaces would suffice to show the capabilities of the robots ability

to adhere to steel surfaces commonly found on steel bridges. Demonstration of the robot deployments is given in this link: <https://youtu.be/8d78d7CWXYk>

As Figs. 8, 9, 10, 11 show, the robot was able to adhere to the steel I beams successfully. From here, we subjected the



Fig. 11: Robot testing on flat steel structures and passing external corner.



Fig. 12: Camera views serve for monitoring visual defect.

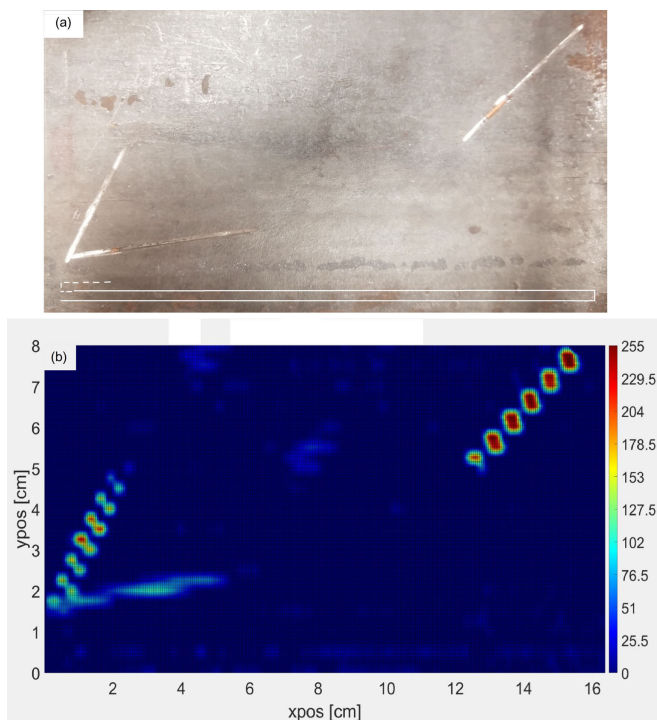


Fig. 13: The presented data in an indoor experiment on $8 \times 16\text{cm}$ steel surface with artificial cracks. The probe path is illustrated as white color lines covering the entire surface (a). Data includes Eddy current sensor signal data (z, db) and probe position (x,y, cm). x,y,z is saved in .csv extension with sample time is 0.1s. The heat map is created to represent the data with MATLAB (b). Red (serious fatigue crack area), Yellow (moderate fatigue crack area), and Blue (good area: no crack).

ARA robot to a few cases of field abuse by pushing, shoving, and prying the robot in various manners with little success in budging it. In order to get the robot off of a steel surface, we had to make the robot roll onto a plate that separated the robot from the steel. After this, we removed the robot from the steel surface by using the plate like a wedge.

From these surfaces, the robot also obtained data from scanning with the eddy current sensor. The corresponding heat maps from the indoor field test are as follows. While scanning, the robot records data from the eddy current sensor, the IMU, and the camera to generate an easy-to-read heatmap as shown in Fig. 13.

The proposed robot can adhere to cylindrical surfaces horizontally and traverses along nearly all continuous steel surfaces, commonly found on steel bridges throughout the world. The robot can withstand a significant amount of misuse and ensures that the expensive equipment housed on the robot will not be lost when operating.

A. Data collection

We could use these opportunities to gather some data on the steel that the robot was placed onto with the eddy current sensor. Once this data was retrieved, we created a heat map of the eddy current data of the steel surfaces that the robot had scanned. This allows the collected data to be reviewed quickly and intuitively, which does not take extensive knowledge of steel to assess. The created robot would allow a technician to complete a detailed and thorough inspection of a steel bridge or structure without a need for a deep knowledge of steel.

V. CONCLUSION AND FUTURE WORK

A new robot designed, created, and presented in this paper is a high-strength, high mobility robot capable of utilizing embedded equipment to conduct nondestructive evaluation and gather data. An in-depth analysis of the robot was undertaken to calculate and discern the limits of the design mathematically. This yielded the failure characteristics of the robot and allowed us to characterize the degree to which the designed robot can withstand real-world stimulus and abuse. Our goal has been to help the inspectors meet the growing demand for bridge inspections on civil infrastructure. To

meet this task, we have constructed a robot, which is durable, reliable, and capable of performing the nondestructive evaluation. Overall, the robot will improve the efficiency and quality of steel bridge inspectors equipped with it.

Future work could include the integration of simultaneous localization and mapping, an informed redesign, and an integrated screen and GUI to assist with ensuring the robot can easily be used by technicians. We have also considered designing a modular attachment to oscillate the eddy current sensor at a frequency fast enough to effectively retrieve a line of data at some time instead of a point of data. We would also like to make use of image stitching (developed in the previous work [35]) to put together camera images taken and the heat maps generated with some transparency such that the two images could be overlaid onto each other for even easier and time efficient identification of damaged or degrading steel.

REFERENCES

- [1] "U.S DEPARTMENT OF TRANSPORTATION HIGHWAY ADMINISTRATION, NATIONAL BRIDGE INVENTORY DATA, 2019, howpublished = <http://www.fhwa.dot.gov/bridge/nbi.cfm>."
- [2] H. Ahmed, H. M. La, and N. Gucunski, "Review of non-destructive civil infrastructure evaluation for bridges: State-of-the-art robotic platforms, sensors and algorithms," *Sensors*, vol. 20, no. 14, 2020. [Online]. Available: <https://www.mdpi.com/1424-8220/20/14/3954>
- [3] ASCE, "2017 infrastructure report card," <https://www.infrastructurereportcard.org/wp-content/uploads/2017/01/Bridges-Final.pdf>, 2017.
- [4] Source: <https://www.cbsnews.com/news/golden-gate-bridge-san-francisco-engineers-take-detailed-look/>.
- [5] C. Balaguer, A. Giménez, J. M. Pastor, V. M. Padron, and M. Abderrahim, "A climbing autonomous robot for inspection applications in 3d complex environments," *Robotica*, vol. 18, no. 3, pp. 287–297, 2000.
- [6] D. Zhu, J. Guo, C. Cho, Y. Wang, and K. Lee, "Wireless mobile sensor network for the system identification of a space frame bridge," *IEEE/ASME Trans. on Mechatronics*, vol. 17, no. 3, pp. 499–507, June 2012.
- [7] G. Lee, G. Wu, J. Kim, and T. Seo, "High-payload climbing and transitioning by compliant locomotion with magnetic adhesion," *Robotics and Autonomous Systems*, vol. 60, no. 10, pp. 1308 – 1316, 2012. [Online]. Available: <http://www.sciencedirect.com/science/article/pii/S0921889012000930>
- [8] T. Seo and M. Sitti, "Tank-like module-based climbing robot using passive compliant joints," *IEEE/ASME Transactions on Mechatronics*, vol. 18, no. 1, pp. 397–408, Feb 2013.
- [9] R. Wang and Y. Kawamura, "A magnetic climbing robot for steel bridge inspection," in *Proceeding of the 11th World Congress on Intelligent Control and Automation*, June 2014, pp. 3303–3308.
- [10] J. Guo, W. Liu, and K. M. Lee, "Design of flexonic mobile node using 3d compliant beam for smooth manipulation and structural obstacle avoidance," in *2014 IEEE Intern. Conf. on Robotics and Automation (ICRA)*, May 2014, pp. 5127–5132.
- [11] S. Kamdar, "Design and manufacturing of a mecatron sheel for the magnetic climbing robot," *Master Thesis, Embry-Riddle Aeronautical University*, May 2015.
- [12] P. Ward, P. Manamperi, P. R. Brooks, P. Mann, W. Kaluarachchi, L. Matkovic, G. Paul, C. H. Yang, P. Quin, D. Pagano, D. Liu, K. Waldron, and G. Dissanayake, "Climbing robot for steel bridge inspection: Design challenges," in *Austroroads Publications Online, ARRB Group*, 2015.
- [13] R. Wang and Y. Kawamura, "Development of climbing robot for steel bridge inspection," *Industrial Robot: An International Journal*, vol. 43, no. 4, pp. 429–447, 2016. [Online]. Available: <https://doi.org/10.1108/IR-09-2015-0186>
- [14] N. H. Pham, H. M. La, Q. P. Ha, S. N. Dang, A. H. Vo, and Q. H. Dinh, "Visual and 3d mapping for steel bridge inspection using a climbing robot," in *The 33rd Intern. Symposium on Automation and Robotics in Construction and Mining (ISARC)*, July 2016, pp. 1–8.
- [15] R. Wang and Y. Kawamura, "An automated sensing system for steel bridge inspection using gmr sensor array and magnetic wheels of climbing robot," *Journal of Sensors*, vol. 2016, 2016.
- [16] Y. Takada, S. Ito, and N. Imajo, "Development of a bridge inspection robot capable of traveling on splicing parts," *Inventions*, vol. 2, 2017. [Online]. Available: <http://www.mdpi.com/2411-5134/2/3/22>
- [17] M. Eich and T. Vögele, "Design and control of a lightweight magnetic climbing robot for vessel inspection," in *the 19th Mediterranean Conf. on Control Automation*, June 2011, pp. 1200–1205.
- [18] P. J. Sanchez-Cuevas, P. Ramon-Soria, B. Arrue, A. Ollero, and G. Heredia, "Robotic system for inspection by contact of bridge beams using uavs," <https://www.mdpi.com/1424-8220/19/2/305/htm>, 2019.
- [19] G. La Rosa, M. Messina, G. Muscato, and R. Sinatra, "A low-cost lightweight climbing robot for the inspection of vertical surfaces," *Mechatronics*, vol. 12, no. 1, pp. 71 – 96, 2002. [Online]. Available: <http://www.sciencedirect.com/science/article/pii/S0957415800000465>
- [20] N. H. Pham and H. M. La, "Design and implementation of an autonomous robot for steel bridge inspection," in *54th Allerton Conf. on Comm., Con., and Comp.*, Sept 2016, pp. 556–562.
- [21] H. M. La, T. H. Dinh, N. H. Pham, Q. P. Ha, and A. Q. Pham, "Automated robotic monitoring and inspection of steel structures and bridges," *Robotica*, vol. 37, no. 5, pp. 947 – 967, May 2019.
- [22] S. T. Nguyen and H. M. La, "Development of a steel bridge climbing robot," in *2019 IEEE/RSJ International Conference on Intelligent Robots and Systems (IROS)*, 2019, pp. 1912–1917.
- [23] —, "Roller chain-like robot for steel bridge inspection," in *In proceedings of the 9th International Conference on Structural Health Monitoring of Intelligent Infrastructure (SHMII-9)*, August 4-7, St. Louis, Missouri, USA, 2019.
- [24] A. Q. Pham, H. M. La, K. T. La, and M. T. Nguyen, "A magnetic wheeled robot for steel bridge inspection," in *Advances in Engineering Research and Application*, K.-U. Sattler, D. C. Nguyen, N. P. Vu, T. L. Banh, and H. Puta, Eds. Cham: Springer International Publishing, 2020, pp. 11–17.
- [25] S. T. Nguyen, A. Q. Pham, C. Motley, and H. M. La, "A practical climbing robot for steel bridge inspection," in *2020 IEEE International Conference on Robotics and Automation (ICRA)*, 2020, pp. 9322–9328.
- [26] H.-D. Bui, S. T. Nguyen, U.-H. Billah, C. Le, A. Tavakkoli, and H. M. La, "Control framework for a hybrid-steel bridge inspection robot," in *IEEE/RSJ International Conference on Intelligent Robots and Systems (IROS)*, 2020.
- [27] H.-D. Bui and H. M. La, "Navigation framework for a hybrid steel bridge inspection robot," in *arXiv, cs.RO, 2101.02282*, 2021.
- [28] S. T. Nguyen, H. Nguyen, S. T. Bui, V. A. Ho, and H. M. La, "Multi-directional bicycle robot for steel structure inspection," in *arXiv, cs.RO, 2103.1152*, 2021.
- [29] S. T. Nguyen and H. M. La, "A climbing robot for steel bridge inspection," *Journal of Intelligent and Robotic Systems*, vol. 102, no. 75, 2021.
- [30] C. Motley, S. Nguyen, and H. M. La, "Design of a high strength multi-steering climbing robot for steel bridge inspection," in *2022 IEEE/SICE International Symposium on System Integration (SII)*, Narvik, Norway, January 8-12, 2022.
- [31] D. Pagano and D. Liu, "An approach for real-time motion planning of an inchworm robot in complex steel bridge environments," *Robotica*, vol. 35, no. 6, p. 1280–1309, 2017.
- [32] P. Quin, G. Paul, A. Alempijevic, and D. Liu, "Exploring in 3d with a climbing robot: Selecting the next best base position on arbitrarily-oriented surfaces," in *2016 IEEE/RSJ International Conference on Intelligent Robots and Systems (IROS)*, 2016, pp. 5770–5775.
- [33] G. Paul, P. Quin, A. W. K. To, and D. Liu, "A sliding window approach to exploration for 3d map building using a biologically inspired bridge inspection robot," in *2015 IEEE International Conference on Cyber Technology in Automation, Control, and Intelligent Systems (CYBER)*, 2015, pp. 1097–1102.
- [34] Zhu, "Tutorial on hertz contact stress," <https://wp.optics.arizona.edu/optomech/wp-content/uploads/sites/53/2016/10/OPTI-521-Tutorial-on-Hertz-contact-stress-Xiaoyin-Zhu.pdf>, December 2012.
- [35] H. M. La, N. Gucunski, S.-H. Kee, and L. Nguyen, "Data analysis and visualization for the bridge deck inspection and evaluation robotic system," *Visualization in Engineering*, vol. 3, no. 1, pp. 1–16, 2015.